scientific reports

Check for updates

OPEN

A heat-flux upper boundary for modeling temperature of soils under an embankment in permafrost region

Tianyu Wang[1,2]✉ & Li-E. Yan[1,2]

Building roads in permafrost region is challenged because permafrost is sensitive to temperature increase. As an embankment gains/drains heat mostly at the upper surface, accurately modeling the heat transfer in the upper surface is crucial to understand the thermal stability of the road. Popular methods treat the upper boundary as a temperature-controlled model (TCM), where temperature of the upper surface is set as a sinusoidal function. This simple function, however, fails to identify the influences of solar irradiance, heat convection, and thermal irradiance on the heat transfer on the ground surface. Here we introduce a heat-flux model (HFM) to calculate the heat fluxes at the embankment upper surface and at the adjacent ground surface. HFM-predicted temperature under an embankment is compared against the observed temperature to validate the model, and is compared to the TCM-predicted temperature. While TCM-predicted temperatures and HFM-predicted ones are similar in trend and in pattern, the HFM-predicted temperatures are far more coincident with the observed ones. The pros and cons of both HFM and TCM are discussed. Further studies are expected to use HFM to understand the heat flux components such as solar absorption, heat convection, and thermal irradiance on the temperature of permafrost under embankments.

List of symbols

English symbols

T	Temperature (°C)
T_s	Ground-surface temperature (°C)
T_a	Air temperature (°C)
T_d	Dew point temperature (°C)
T_e	Bottom limit temperature (°C)
T_f	Upper limit temperature (°C)
T_0	Mean annual temperature (°C)
c	Heat capacity (J/(kg·K))
c_{eq}	Equilibrium heat capacity (J/(kg·K))
t	Time (s)
A	Amplitude of the temperature (°C)
I	Solar irradiance (W/m^2)
I_b	Beam irradiance (W/m^2)
I_{bs}	Beam irradiance on the side slope (W/m^2)
I_{bg}	Beam irradiance on the ground (W/m^2)
I_d	Diffuse irradiance (W/m^2)
I_{ds}	Diffuse irradiance on the side slope (W/m^2)
I_{dg}	Diffuse irradiance on the ground (W/m^2)
I_s	Solar irradiance on the side slope (W/m^2)
R	Reflectance (–)
L	The net long-wave radiation (W/m^2)

[1]College of Civil Engineering and Architecture, Guangxi University, 100 University Road, Nanning 530004, Guangxi, China. [2]The Key Laboratory of Disaster Prevention and Structural Safety of Ministry of Education, Guangxi University, Nanning 530004, China. ✉email: tywang09@163.com

L_d	Downward thermal irradiance (W/m^2)
L_u	Upward long-wave radiation (W/m^2)
H	Heat convection (W/m^2)
E	Evaporation (W/m^2)
G	Conduction (W/m^2)
h_c	Heat convection coefficient (W/(m·°C))
v	Wind speed (m/s)
z	Height (m)
N	Day number of the year (–)
k_y	Sky cleanness factor (–)
h	Height of the embankment (m)
x_0	Width of the shaded area (m)
$F_{x\rightarrow sky}$	Sky view factor (–)
w	Water content (–)
L_w	Latent heat of water (kJ/kg)

Greek symbols

ρ	Density (kg/m^3)
λ	Heat conductivity (W/(m·K))
ε	Thermal emissivity (–)
σ	Stefan–Boltzmann constant (–)
χ	Relative humidity (–)
β	Latitude (rad)
δ	Solar declination angle (rad)
α	Solar hour angle (rad)
θ	Solar zenith angle (rad)
γ	Solar azimuth angle (rad)
γ_e	Orientation of the embankment (rad)
η	Angle of the side slope (rad)
ψ	Azimuth of the side slope (rad)
ω	Angular frequency (rad/s)
ϕ	Phases (rad)

Subscripts

us	Unfrozen soil
fs	Frozen soil
w	Water
u	Unfrozen water
i	Ice
y	Sky

Abbreviations

NG	Natural ground surface
S	Side slope
SS	South-facing side slope
NS	North-facing side slope
QTH	Qinghai-Tibet Highway
QTR	Qinghai-Tibet Railway
QTP	Qinghai-Tibet Plateau

Permafrost regions cover approximately 22.8 million km^2 earth surface, of which permafrost in China makes up 1.59 million km^2[1]. Roadways across permafrost regions are usually layered upon a built-up embankment to keep the underlying soil intact[2]. The construction of the embankment varies the permafrost stratum undesirably and causes differential settlement at the ground surface[3–6]. Accurately simulating the heat transfer at the ground surface is critical to precisely predict the temperature of the permafrost stratum after the construction of the embankment. When simulating the temperature of soils under a permafrost embankment, popular methods usually treat this boundary as a temperature-control model (TCM)[7–9], in which the temperature at the ground surface is assumed a sinusoidal wave. This sinusoidal wave is used to bulkily represent the influences of solar radiation, heat convection, thermal irradiance, and evaporation (if any) on the ground surface[10]. While this model is simple, the parameters of the sinusoidal wave are estimated by rule of thumb, but not by art (Table 3) and is thus hard to be estimated accurately.

If the ground-surface temperature can be guessed reliably, the temperatures of the deeper soil vary less and thus can be estimated with greater confidence. Qin et al. has proposed a heat-flux upper boundary (HFUB) for the natural ground surface to predict the temperature of permafrost stratum[10,11]. The model is suitable to predict the temperature of permafrost under a flat, open area only. Liu et al. then proposed an earth-atmosphere coupled model to predict the temperature of soil under an embankment[12]. This model, however, does not consider the

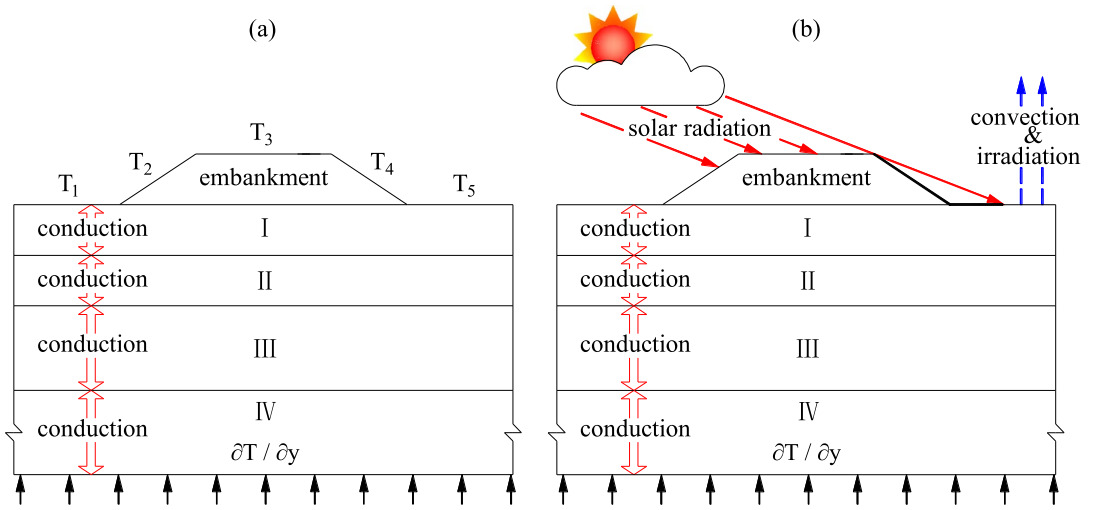

Figure 1. The computational domain of an embankment underlain by permafrost. (**a**) temperature-controlled upper boundary, (**b**) heat-flux upper boundary. T_i ($i = 1, 2, \ldots, 5$) stands for a specific sinusoidal temperature function.

variation of daily solar irradiance. Without a HFM for predicting the temperature of the embankment and its underlying soils, it is unscientific to guide the selection of performance grading of asphalt binder for asphalt pavement under the specific climate condition; it is difficult to understand the partition of radiant heat flux at the ground and to find practical solutions that cut the heat gain of the embankment to preserve the underlying permafrost; it is unknown how to eliminate the sunny-shady effect of embankment in permafrost region by equalizing the conductive heat at both embankment side slopes. In addition, as the global warming heats up the underlying permafrost and causes deformation to the embankment, the HFM is indispensable to predict the settlement of the embankment precisely.

Here we propose a comprehensive heat-flux model (HFM) for the heat transfer at the embankment upper surface and at the natural ground adjacent to the embankment. The proposed model considers the heat flux from solar irradiance, heat convection, and thermal irradiance, and counters the shading effect of the embankment on the adjacent ground. Temperatures predicted by the HFM model are compared against the temperature profiles that are observed from a testing section at the Beiluhe Permafrost Station in the Qinghai-Tibet Plateau. The TCM is also used to predict the temperature at the same site to demonstrate the difference between the TCM and the HFM. The pros and cons of both the HFM and the TCM are explained. The application of the HFM is briefly discussed.

Numerical models

The heat transfer in the embankment and in the soils below an embankment is conduction-dominated, which obeys

$$\rho c_{eq} \frac{\partial T}{\partial t} = \nabla \cdot (\lambda \nabla T) \tag{1}$$

where ρ (kg/m^3) is the density of the soils; T (°C) is the temperature of the soils; c_{eq} (J/(kg K)) is the equilibrium heat capacity of the soils; and λ (W/(m·K)) is the heat conductivity of the soil. It is noted that c_{eq} represents the latent heat of the permafrost when the phase change of water in the permafrost occurs. Methods to calculate c_{eq} and λ have been documented well and can be referred in Appendix A of Supplementary Information.

To solve Eq. (1), one must specify a proper boundary condition to the computational domain, which should be sufficiently large so that a further extent of the domain does not influence the temperature simulation of the embankment and of the underlying soils. As an embankment is usually an isosceles trapezoid with the short base at the top, the computational domain is selected as the trapezoid centered over a rectangle envelop that represents the natural ground (Fig. 1). The heat flux from right and left sides of the rectangle envelop is adiabatic, and the heat flux from the bottom of the base is the product of the local geothermal gradient and the heat conductivity of the soil at the base (Fig. 1). Most of heat fluxes that change the temperature of the embankment and of the underlying soils come from the upper boundary, which consist of the embankment upper surface, the side slope surface, and the adjacent natural ground surface (Fig. 1). In published articles[10,13], the upper boundary can be treated as either a temperature-controlled boundary (Fig. 1a) or a heat-flux boundary (Fig. 1b).

Temperature-controlled model (TCM). Popular models to predict the temperature of the permafrost under a roadway embankment prefer using a temperature boundary, which is termed TCM. The TCM specifies to the upper boundary as a sinusoidal temperature function

$$T_s = T_0 + A\cos(\varpi t + \phi) \tag{2}$$

where T_s (°C) is the ground-surface temperature, T_0 (°C) represents the mean annual ground temperature, and A (°C) is the amplitude of the ground-surface temperature, ω (rad/s) represents the angular frequency, $\omega = 2\pi/(24 \times 3600 \times 365)$; and ϕ stands for the phases (in radians) of annual ground surface temperature.

Equation (2) considers the daily temperature only, although some models occasionally take the daily temperature pattern into account[14]. As the ground-surface temperature is difficult to be measured directly, T_0 and A are coarsely estimated from the annual air temperature (data from the nearly weather station) according to the adhesive layer theory[15]. Parameters in Eq. (2) bulkily represent the complex heat transfer at the ground surface, without considering the solar irradiance, convection, thermal irradiance, and evaporation.

Heat-flux model (HFM). *Heat flux at boundary of the computational domain.* The HFM focuses on formulating the upper boundary to solve the temperature of soils in the computational domain using Eq. (1). The most variable heat-flux boundaries are the ground surfaces and the embankment's upper surface. Both surfaces absorb irradiance from the sun and downward thermal irradiances from the outer space L_d (W/m^2). Both surfaces release a portion of the absorption as heat convection H (W/m^2), upward long-wave radiation to the outer space L_u (W/m^2), and evaporation E (W/m^2) (if any) simultaneously. The surplus heat flux, G (W/m^2), stores at the ground surface to vary the skin temperature and conducts it to the deeper soils. The heat balance of the upper surface exposed to the air obeys,

$$I(1 - R) + L_d = G + H + L_u + E \tag{3}$$

where I (W/m^2) is the incoming solar irradiance to the surface, R (–) is the reflectance (albedo) of the surface.

In Eq. (3), L_u and L_d are proportional to the ground-surface thermal emissivity, ε (–); in practice, it is more convenient to compute the net long-wave radiation, which is

$$L = L_u - L_d = \varepsilon\sigma\left((T_s + 273.15)^4 - \left(T_y + 273.15\right)^4\right) \tag{4}$$

where σ is the Stefan-Boltzmann constant, $\sigma = 5.67 \times 10^{-8}$ W $\cdot$m^{-2} $\cdot$K^{-4}; the subscripts "s" and "y" represent the ground surface and the outer sky, respectively.

In Eq. (4), the ground-surface temperature, T_s, can be calculated from Eq. (1) once the heat flux is specified to the boundary of the computational domain. The sky temperature, T_y (°C), can be estimated:

$$T_y = \varepsilon_y^{0.25}(T_a + 273.15) - 273.15 \tag{5}$$

where T_a (°C) is the air temperature; ε_y (–) is the sky emissivity, which is

$$\varepsilon_y = 0.754 + 0.0044T_d \tag{6}$$

where T_d (°C) is dew point:

$$T_d = b_0 r_0/(a_0 - r_0) \tag{7}$$

where $a_0 = 17.3$, $b_0 = 237.7$, and $r_0 = a_0 T_a/(b_0 + T_a) + \ln(\chi/100)$[12], with χ is the relative humidity of the surrounding air.

The heat convection, H, can be calculated by

$$H = h_c(T_s - T_a) \tag{8}$$

where h_c (W/(m^2·°C)) is the heat convection coefficient. The computation of h_c has been well documented in many models, among which the following simple one can provide reliable accuracy[16]

$$h_c = \begin{cases} 5.6 \times 4.0v & v < 5 \\ 7.2 \times v^{0.78} & v \geq 5 \end{cases} \tag{9}$$

where v (m/s) is the wind speed recorded at a height of 9.0 m. For a wind recorded from a weather station that is not set at 9.0 m height, the wind speed must be converted according to

$$v = v_z\left(\frac{z}{9}\right)^{\frac{1}{7}} \tag{10}$$

In Eq. (3), the evaporation E is difficult to calculate because it is hard to know both the water availability at the ground surface and the evaporation resistance of the ground surface. When water is available at the ground surface, the evaporation is proportional to the incoming solar radiation, with the peak evaporation occuring around solar noon and with a negligible evaporation at nighttime. According to Qin et al.[10], the evaporation term can be reasonably neglected by calibrating the solar reflectance at the ground surface. In this model, the evaporation is neglected, and the ground-surface reflectance is adjusted unless the observed ground temperature is coincident with the predicted one. As a result, the heat flux to the upper boundary of the computational domain is

$$G = I(1 - R) - H - L \tag{11}$$

Sunlit and shade of the side slope of an embankment. In Eq. (11), formulas to calculate the components H and L have been shown. The most complex component in Eq. (11) is the solar irradiance, I, on the embankment surface and on the ground surface adjacent to the embankment.

Solar irradiance on a global horizontal surface is the global horizontal solar irradiance logged from the local weather station. Solar irradiance is partitioned to beam radiation and diffuse radiation. The side slope of an embankment can be either shaded or sunlit, depending on the time of the day, on the day number of the year, on the orientation of the embankment, and on the angle of the side slope. The solar irradiance on the side slope is thus more complicate. To find the solar irradiance on a tilt surface, one must find the solar azimuth angle, which varies with day and time. On a specific day, the solar declination angle, δ (rad), can be estimated from

$$\delta = 0.409\sin(2\pi\frac{N+284}{365}) \tag{12}$$

where N is the day number of the year, with $N=1$ on January 1.

On a specific time of the day, the solar zenith angle can be estimated from

$$\cos\theta = \sin\delta\sin\beta + \cos\delta\cos\beta\cos\alpha \tag{13}$$

where β (rad) is the latitude of the observer; α (rad) is the solar hour angle, which is 0 at solar noon. The time span from sunrise to sunset can be derived from:

$$\cos\alpha = \frac{\sin(-0.83^\circ) - \sin\delta\sin\beta}{\cos\beta\cos\delta} \tag{14}$$

where α at the sunset time is positive, and at the sunrise time is negative.

With the solar declination angle, the solar zenith angle and the solar hour angle, one can find the solar azimuth angle, γ (rad), is given by

$$\sin\gamma = \cos\delta\sin\alpha/\sin\theta \tag{15}$$

If $|\sin\gamma| > 1$ or if $|\sin\theta|$ in Eq. (15) is infinitesimal, the solar azimuth angle has to be estimated by:

$$\cos\gamma = \frac{\cos\theta\sin\beta - \sin\delta}{\sin\theta\cos\beta} \tag{16}$$

It is noted that at noon $\theta=0$, the denominator in Eqs. (15) and (16) is equal to zero. To circumvent this problem, one can discrete the time sequence between sunrise to sunset in an even number so that the sequence does not have $\theta=0$.

With the solar azimuth angle, one can determine if a side slope of an embankment is sunlit or shaded. At low-sun case, beam radiation hits one side slope only, while the other is shaded. Assuming the height of the embankment is h (m), beam radiation creates a shaded belt parallel with the embankment orientation. The width of the belt is

$$x_0 = h\tan\theta\cos(\gamma - \gamma_e) \tag{17}$$

where γ_e (rad) is the orientation of the embankment.

Whether a side slope of an embankment is sunlit or shaded can be estimated by

$$\begin{cases} x_0 \geq h\cot(\eta) & \text{south/east} - \text{facingsideslopeisshaded} \\ x_0 \leq -h\cot(\eta) & \text{north/west} - \text{facingsideslopeisshaded} \\ -h\cot(\eta) < x_0 < h\cot(\eta) & \text{bothsideslopesissunlit} \end{cases} \tag{18}$$

where η (rad) is the angle of the side slope of the embankment.

Solar irradiance on the upper surface of the computational domain. Global solar horizontal solar irradiance, I (W/m^2), is divided into beam irradiance I_b (W/m^2) and diffuse irradiance I_d (W/m^2), that is

$$I = I_d + I_b \tag{19}$$

The division has been documented in many models, in which one simple, well-cited model can provide reasonable accuracy[17]:

$$\frac{I_d}{I} = \begin{cases} 1.0 - 0.249k_y, k_y < 0.35 \\ 1.557 - 1.84k_y, 0.35 \leq k_y \leq 0.75 \\ 0.177k_y > 0.75 \end{cases} \tag{20}$$

where k_y is the sky cleanness factor with 0 representing a fully cloudy day and 1.0, a fully sunny day.

The global horizontal solar irradiance, I, can be directly specified to the upper surface of the embankment. However, the solar irradiance on the side slope and on the natural ground surface adjacent to the embankment is more complicate. According to Eq. (18), if a surface is sunlit, the solar irradiance is $I_d + I_b$ falling on that surface; otherwise, is the I_d only. Diffuse irradiance on the side slope is

$$I_{ds} = I_d(1 + \cos\eta)/2 \tag{21}$$

Layer	ρ (kg/m^3)	w (%)	a	b	k (W m^{-1} K^{-1})		c (J kg^{-1} K^{-1})	
					k_u	k_f	c_u	c_f
Embankment	2111	8	0.053	0.209	1.433	1.537	1050.5	892.6
I	2227	8	0.021	0.310	1.485	1.525	866.3	856.3
II	2130	12	0.052	0.520	1.449	1.528	991.4	870.8
III	1980	40	0.112	0.519	1.242	1.642	1766.6	1157.3
IV	2180	8	0.053	0.281	1.433	1.537	1050.2	892.9
Water	1000	–	–	–	0.600	2.000	2050.0	4181.3

Table 1. Thermal parameters of the soils in the Beiluhe Permafrost Station. Data can be referred from paper[10]; physical meanings of some parameters are referred to the Appendix A of Supplementary Information.

The beam radiation on the side slope is the dot product of the beam irradiance I_b and the normal of the side slope.

$$I_{bs} = I_b(\sin\theta\sin\eta\cos(\psi - \gamma) + cos\theta\cos\eta) \tag{22}$$

where the azimuth of the side slope, ψ (rad), can be estimated by

$$\begin{aligned} \psi &= \pi - \gamma_e, \text{ face south/east} \\ \psi &= 2\pi - \gamma_e, \text{ face north/west} \end{aligned} \tag{23}$$

In Eq. (22), if $I_{bs} < 0$, which means the slope is shaded, then $I_{bs} = 0$. The solar irradiance on the side slope is

$$I_s = I_{ds} + I_{bs} \tag{24}$$

The solar irradiance on the natural ground surface, I_g, is also the addition of diffuse irradiance I_{dg} and beam irradiance I_{bg}. The construction of the embankment blocks the sky view of the natural ground surface, especially the surface that is close to the side slope toe of the embankment. Setting the side slope toe is the origin, the x axis perpendicular to the embankment orientation, and the y axis normal to the ground surface, one gets the sky view factor of any point $(x,0)$ at the natural ground surface as

$$F_{x\to\text{sky}} = 0.5 + 0.5\frac{h\cot(\eta) + x}{\sqrt{h^2 + (h\cot(\eta) + x)^2}} \tag{25}$$

The diffuse radiation on the natural ground surface adjacent to the side slope is

$$I_{dg} = F_{x\to\text{sky}} I_d \tag{26}$$

The beam radiation on the natural ground surface is

$$I_{bg} = \begin{cases} I_b\cos\theta & \text{sunlit} \\ 0 & \text{shaded} \end{cases} \tag{27}$$

The solar irradiance on the natural ground surface adjacent to the side slope is

$$I_g = I_{dg} + I_{bg} \tag{28}$$

It is noted that a factor of sunlight reflecting from the side slope can be captured by the adjacent natural ground surface, and vice versa. This solar trapping effect increases the solar absorption of the side slope and of the adjacent ground, especially for the surface near the side slope toe. This topic has been documented and it is found the additional solar absorption caused by the solar trapping effect is negligibly small compared to the solar absorption[18].

Simulations information. This study uses both the TCM and HFM to simulate the temperature of underlying permafrost under an embankment in the Beiluhe Permafrost Station (34.8° N, 92.9° E). The simulated results are compared against the logged temperature. The embankment is isosceles with a height of 3 m, a top (short) base of 8.0 m, and a lower (long) base of 17 m. The computational domain is extended horizontally 20 m from the side-slope toe of the embankment, and vertically 22 m from the natural ground surface. The orientation of the embankment is set as east–west orientation, because the thermal asymmetry of this embankment is the most-deleterious case. The embankment filler consists of coarse grained soil. The computational domain in the natural ground, from top to down, consists of a 2 m-thick loose silty clay, a 2 m-thick silty clay, a 6 m-thick layer with ground ice and clay, and finally a 12 m-thick mudstone silty clay (Fig. 1). Soils' thermal parameters used for the simulation are listed in Table 1. Both left and right sides of the computational domain are set as adiabatic, and the thermal gradient at the bottom of the domain is 0.03 °C/m.

Firstly, the heat-flux boundary is specified to the upper surface of the computational domain. The air temperature T_a, the global horizontal solar radiation I, and the wind speed v, the relative humidity χ, and the sky cleanness factor k_y at the embankment site are logged from typical annual weather data. The solar irradiance on

the top of the embankment is Eq. (19); that on the side slope, Eq. (24); and that on the adjacent ground surface, Eq. (28). The solar reflectance of the embankment top, side slope, and adjacent ground is set as 0.22 according to Qin et al.[19]. Considering that water evaporates when it is available at the topsoil and that the evaporation pattern is coincident with solar radiation pattern, the simulation adjusts the reflectance some degree unless the predicted temperatures are best matched with the observed ones.

Then, the TCM is used to simulate the permafrost temperature at the same site. As a guess of the parameters (T_0, A, and ϕ) in Eq. (2) could cause substantial errors, this study does not use the adhesive layer theory to parameterize the average, amplitude, and phase of annual ground-surface temperature. Instead, this study uses the least square fitting method to fit the ground-surface temperatures that are predicted via the HFM. The fitting T_0, A, and ϕ in Eq. (2) are used as the parameters for the TCM to simulate the soil temperature under the embankment, while the soils' thermal properties are kept unchanged.

In numerical simulation, either the HFM or the TCM needs specifying an initial temperature to the embankment and to the soil under the embankment. Initial temperatures of the natural ground soils are obtained by repeatedly using the heat-flux boundary to simulate the ground temperature (without embankment) until the differences of the temperature profile at a specific time of two sequential years are less year 0.01 °C. The temperature profile at 00:00 (hh:mm) on September 30 is treated as the initial temperature because the construction of the embankment is completed around this date usually. The initial temperature of the embankment is set as 2 °C uniformly, as usually used in published articles on this topic. This initial temperature (for the soil and the embankment) is used to simulate the temperature of the soils for 50 years after the construction of the embankment.

The soil temperature predicted by the HFM is compared against the temperature logged an earthen embankment in the Beiluhe Permafrost Station from September 2001 to October 2006. The embankment, DK1136 + 400, is an earthen roadbed of the Qinghai-Tibet Railway. Thermistors were buried inside the embankment central borehole and inside the boreholes rightly below the side slope toes to log the soil temperature. In addition, at the natural ground that was 20 m away from the embankment side slope toe, a borehole was also drilled to log temperature at the natural ground. For convenience, the temperature reported in the following section are the daily mean temperature, unless otherwise noted.

Validation method. Since it was assumed that the ground thermal regime has reached an equilibrium state before the construction of the roadbed. Therefore, to ascertain the ground temperature error caused by the iteration, field-observed temperature from September 7, 2001 to September 7, 2006 was compared with that of simulation. In addition, we adopted the coefficient of determination (R^2), mean value (Mean), and standard deviation (Std) to examine the accuracy of the simulation results, where all three indicators were calculated using MATLAB software. The specific calculation methods are as follows:

$$R^2 = 1 - \sum_{i=1}^{n} \left(T_{o,i} - T_{s,i}\right)^2 / \sum_{i=1}^{n} \left(T_{o,i} - \overline{T_o}\right)^2 \tag{29}$$

$$\text{Mean} = \sum_{i=1}^{n} \left(T_{o,i} - T_{s,i}\right)/n \tag{30}$$

$$\text{Std} = \sqrt{\frac{1}{n}\sum_{i=1}^{n}\left[\left(T_{o,i} - T_{s,i}\right) - \sum_{i=1}^{n}\left(T_{o,i} - T_{s,i}\right)/n\right]^2} \tag{31}$$

where T_o, T_s, $\overline{T_o}$ are the observed temperature, the simulated temperature and the average value of the observed temperature, respectively; n represents the total number of values (n = 1, 2, 3, …), and the subscript i stands for the serial number of the values.

Results

Validation of the HFM. Figure 2a,b show the temperature of the soils at 0.5 m depth under the natural ground that is 20 m away from the embankment side slope. It is found that the predicted temperatures (straight line) are well coincident with the simulated ones (dotted data), with $R^2 = 0.975$, a mean error of 0.134 °C and a standard deviation of 0.702 °C (Fig. 2a,b). This statistical data substantiates that the HFM can well predict the temperature of the permafrost under the embankment. The good agreement between the simulation and the observation can be further substantiated from the temperature profiles in the natural borehole. As shown in Fig. 2c, the predicted temperature profile on April 20, 2002 is well agreed with the observed one. Similarly, in Fig. 2d, the predicted temperature profile is highly coincident with the observed one, with $R^2 = 0.963$, a mean error of 0.029 °C and a standard deviation of 0.056 °C.

We further compare the predicted temperature profiles at the central borehole of the embankment to the observed ones. It is found that the predicted temperature near the embankment upper surface is greatly deviated from the observed one (Fig. 3). This great deviation is because the embankment is assumed to be completed as September 30 and the embankment temperature is assumed as 2 °C uniformly. These assumptions are somewhat unrealistic because the real construction of the embankment takes months and the temperature of the earthen filler is unknown. Despite this great deviation at near the ground surface, the predicted temperatures at deeper layer are well agreed with the observed ones (Fig. 3). As the heat of the embankment drains overtime and the

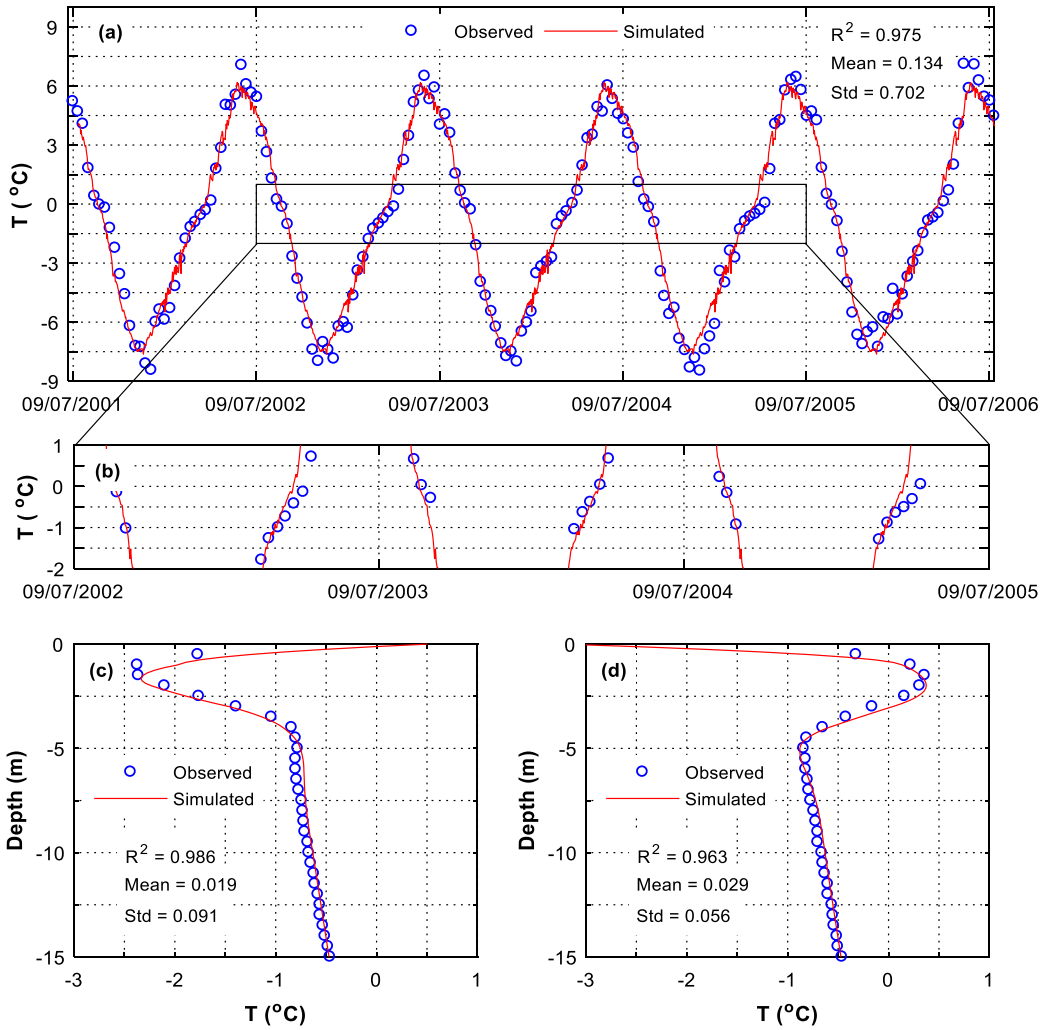

Figure 2. Soil temperature predicted by HFM. Location: at the natural borehole that is 20 m away from the side-slope toe (**a**) temperature serial at 0.5 m depth, with $R^2 = 0.975$, Mean = 0.134 °C and Std = 0.702 °C, (**b**) temperature serial at 0.5 m depth, (**c**) on April 20, 2002, and (**d**) on October 19, 2002.

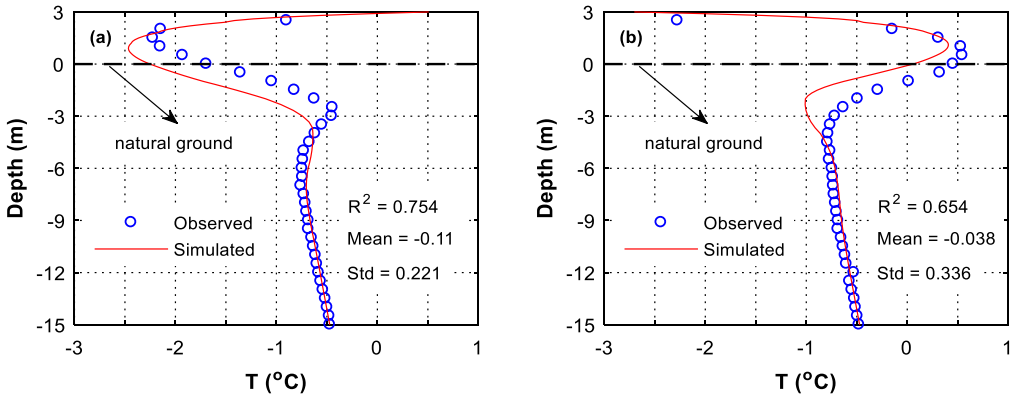

Figure 3. Soil temperature predicted by HFM. Location: at the central borehole. (**a**) on April 20, 2002, and (**b**) on October 19, 2002.

Location	T_0 (°C)	A	ϕ	R^2
Natural ground surface	− 0.76	8.04	1.03π	0.97
Upper surface	− 0.76	8.16	1.03π	0.97
Southern side slope	− 0.60	6.53	1.09π	0.93
Northern side slope	− 2.40	7.58	1.08π	0.96

Table 2. A serial of guess values for T_0 and A, ϕ.

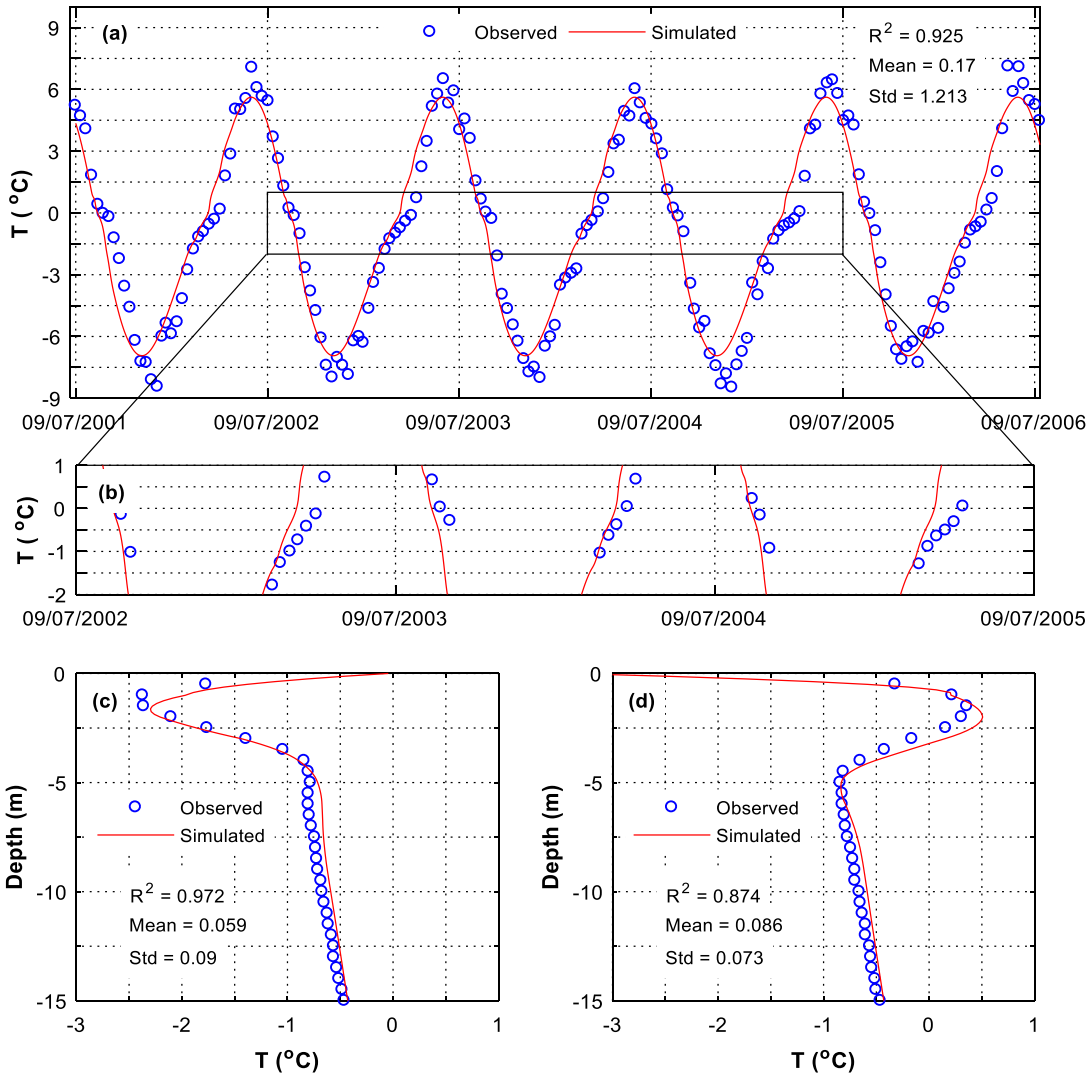

Figure 4. Soil temperatures predicted by TCM. Location: at the natural borehole that is 20 m away from the side-slope toe. (**a**) Temperature serial at 0.5 m depth, with $R^2 = 0.925$, Mean = 0.17 °C and Std = 1.213 °C, (**b**) temperature serial at 0.5 m depth, (**c**) on April 20, 2002, and (d) on October 19, 2002.

influence of the initial temperature on the simulation vanishes, it is believed that the HFM can well predict the temperature of the soil under the embankment.

Comparison of the HFM against the TCM. Here we compare the soil temperatures predicted by the TCM against the observed ones. To impose the TCM to the embankment surfaces, one must know T_0, A, and ϕ in Eq. (2). In this study, the least square fitting method is used to fit the HFM-predicted ground-surface temperature to get T_0, A, and ϕ in Eq. (2). The values of T_0, A, and ϕ tabulated in Table 2 are used, while the others are the same as those used in the HFM.

It is found that the TCM can also predict the temperature of the soil under the natural ground. As shown in Fig. 4a,b, the temperature serial at 0.5 m depth is well coincident with the observed one, with a R square of 0.925, a mean error of 0.17, and a standard deviation of 1.213 °C. A close comparison between the predicted and

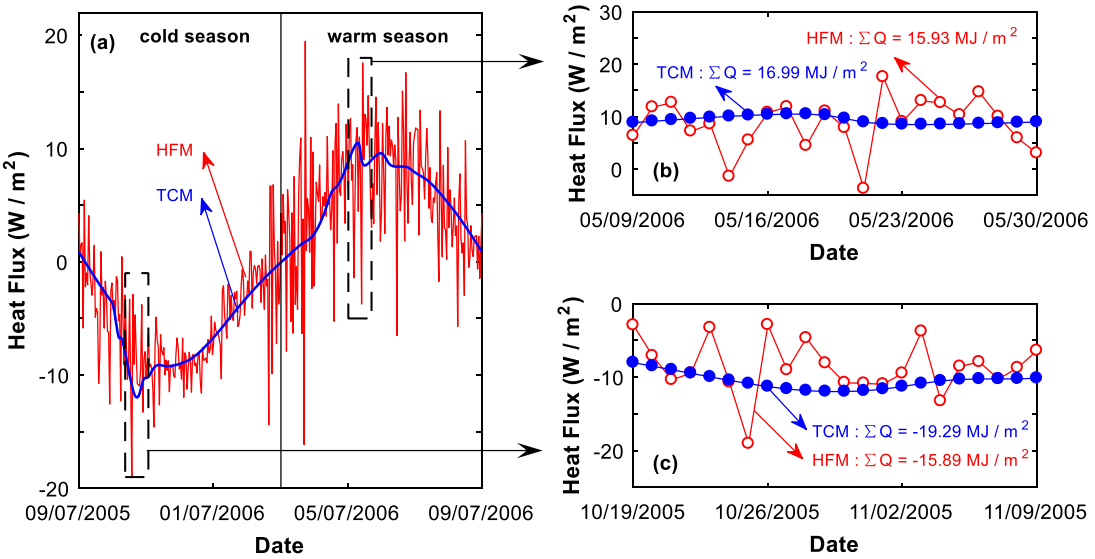

Figure 5. During the freezing/thawing period, the TCM imposes more energy to the natural ground surface than the HFM does. (**a**) The entire year, (**b**) the thawing period, and (**c**) the freezing period.

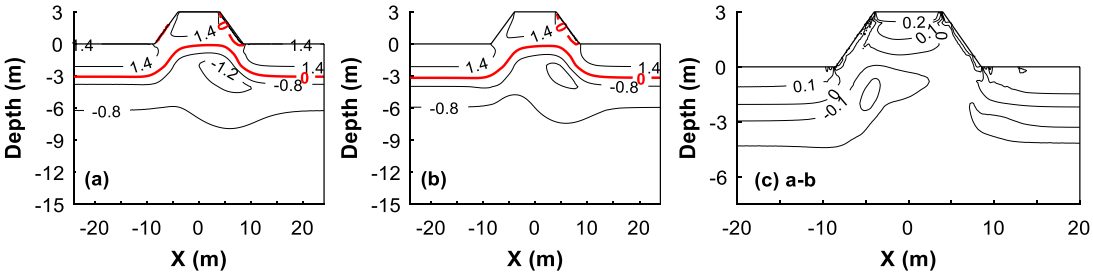

Figure 6. Comparison between the HFM-predicted temperatures and TCM-predicted ones after the embankment is constructed for 5 years. Date: On October 19. (**a**) HFM-predicted temperature, (**b**) TCM-predicted temperature, and (**c**) the HFM-predicted temperatures to minus the TCM-predicted ones.

observed temperatures reveals that when the temperature is close to the freezing/ thawing point (− 1 to 0 °C), the predicted temperature serial increases or decreases faster than the observed one (Fig. 4b). In reality, when the temperature of a soil is close to the freezing/thawing point, the soil needs more heat (cold) to increase (decrease) its temperature (Fig. 5a). But the TCM unrealistically supplies the sufficient heat (cold) to the soil such that the temperature at the ground surface follows a sinusoidal function (Fig. 5b,c). As a result, the TCM-predicted temperatures deviate somewhat from the observed ones, especially for temperature of the soils at shallow ground where they weather cyclic thawing and freezing annually (Fig. 4c,d). At deeper ground where the soil remains frozen, the predicted temperatures are well agreed with the predicted ones (Fig. 4c,d).

As the temperature profiles and temperature serial in the natural boreholes and central borehole cannot represent the temperature of the entire embankment. Here we show the embankment's temperature contours that are predicted by the HFM and the TCM, respectively. In case that the embankment has been built for five years, the daily mean temperature predicted by the HFM, in pattern and in magnitude, are highly similar with those predicted by the TCM (Fig. 6a,b). Using the HFM-predicted temperatures to minus the TCM-predicted ones, one can find the difference between the two modelings is about 0.1–0.2 °C (Fig. 6c), which is negligibly small and further implies that both models can predict the temperature of the soil under the embankment. Similar differences and similar patterns are found when the predicted embankment's temperature contours in 10th year and 50th year are compared (Appendix B in Supplementary Information).

To further understand the difference between the two models, we analyze the temperature profiles at the embankment central borehole and at the southern and northern side-slope toes. It is found that at the central borehole, the temperature profile predicted by the HFM is closely matched with that predicted by the TCM, especially within 5 year after the construction of the embankment (Fig. 7a). Almost the same difference is observed when compared is the temperature profiled predicted by the two models at 10 year after the construction of the embankment (Fig. 7b). As time elapses, the TCM-predicted temperature is about 0.1–0.2 °C higher than the HFM-predicted model, especially at the deeper layers (Fig. 7c). Similar differences and similar deviations between the two models are observed at the temperatures under the side slopes toes (Figs. 8 and 9). We do not know

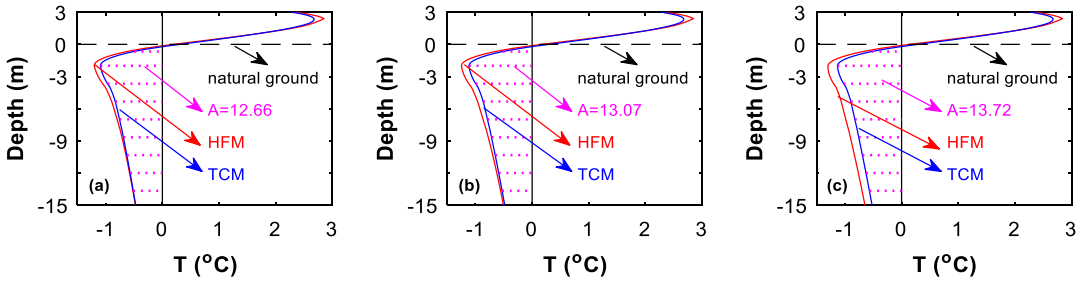

Figure 7. The central-borehole temperature profile predicted by HFM is compared with that by TCM. Date: on October 27. (**a**) 5th year, (**b**) 10th year, and (**c**) 50th year.

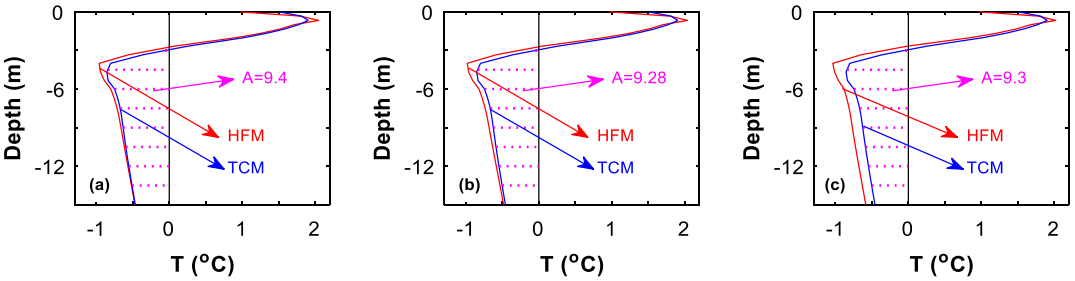

Figure 8. The southern side-slope borehole temperature profile predicted by HFM is compared with that by TCM. Date: on October 27. (**a**) 5th year, (**b**) 10th year, and (**c**) 50th year.

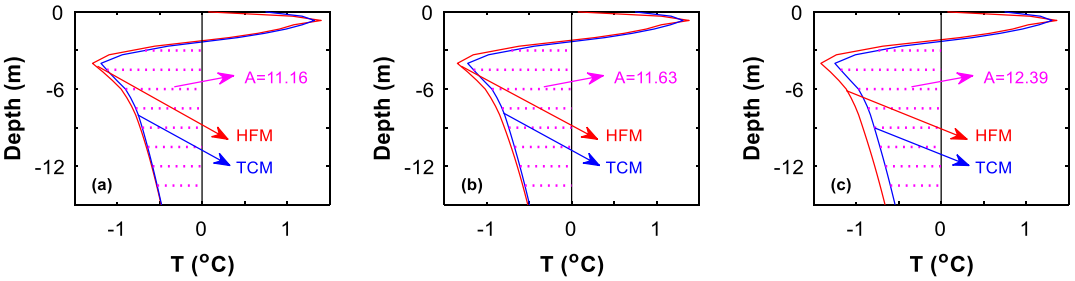

Figure 9. The northern side-slope borehole temperature profile predicted by HFM is compared with that by TCM. Date: on October 27. (**a**) 5th year, (**b**) 10th year, and (c) 50th year.

the reason why the TCM-predicted temperature is about 0.1–0.2 °C higher than the HFM-predicted model, a phenomenon that deserves further investigation.

Discussion

The difference between HFM and TCM. This study is not intended to referee that the HFM is superior to the TCM, or vice versa. Each model has its advantage and disadvantage. The HFM mimics the natural heat transfer at the ground surface and thus can predict the temperature of the soil under the embankment more precisely. The HFM includes the influences of embankment thermal properties and weather data on the temperature of a permafrost stratum. It is thus capable to use the HFM to perform a sensitivity study about the influence of each parameter on the soil temperature. The HFM can help identify if variation of a specific parameter, such as solar reflectance, is favorite to preserve the permafrost under the embankment. If the deformation of the permafrost soil is concerned, it is preferred to use the HFM model to precisely predict the permafrost temperature so that the temperature-related deformation of the soil is estimated properly. In comparison, the TCM model is not a realistic boundary because the ground-surface temperature is not a rigidly sinusoidal wave. The TCM-predicted temperatures could deviate more from the observed ones. But the TCM can predict the temperature of the permafrost in a pattern that is similar to the observed one. As a result, if the trend of the temperature of permafrost under an embankment is interesting, the TCM is superior to the HFM because it is simple and it costs very little simulation time.

Currently, simulation of the temperature of permafrost soils under an embankment needs to guess some parameters. The TCM needs to reasonably guess the mean annual ground-surface temperature, T_0, and the amplitude of this temperature, A. In this study, T_0, A, and ϕ are regressed from the HFM-predicted temperature.

References	Parameters			∂T/∂t (°C/year)	Surfaces	Studies area
	T_0 (°C)	A (°C)	Φ (rad)			
[13]	− 1.5	12	π/2	0.05	NG	An altitude of 4500 m in the QTP
	0.7	13	π/2	0.05	S	
	1.5	15	π/2	0.05	Ballast pavement	
[20]	− 0.4	12	π/2	–	NG	An altitude of over 4500 m in the QTP
	1.8	15	π/2	–	S	
	2.6	15	π/2	–	Ballast pavement	
[21]	− 1.0	12	7π/12	–	NG	An altitude of 4500 m in the QTR
	2.1	13	7π/12	–	SS	
	0.3	13	7π/12	–	NS	
	2.0	15	7π/12	–	Ballast pavement	
[22]	2.3	12.0	π/2	0.05	NG	An altitude of 4500 m along the QTR
	3.3	13.0	π/2	0.05	S	
	4.5	14.0	π/2	0.05	Ballast pavement	
[23]	− 0.5	11.5	π/2	0.02	NG	The Beiluhe basin along the QTR
	1.0	14.5	π/2	0.02	S	
	1.0	14.5	π/2	0.02	Gravel pavement	
[24]	0.4	12.0	π/2	0.05	NG	The Beiluhe basin along the QTP
	− 0.1	14.2	π/2	0.05	S	
	1.0	15.2	π/2	0.05	Ballast pavement	
[25]	− 1.3	12.0	–	0.05	NG	The Beiluhe basin along the QTP
	1.4	13.2	–	0.05	SS	
	− 1.2	15	–	0.05	NS	
	0.4	14.5	–	0.05	Gravel pavement	
[26]	− 0.8	11.5	π/2	0.02	NG	The Beiluhe basin along the QTP
	− 0.7	6.5	π/2	0.02	SS	
	− 1.6	7.5	π/2	0.02	NS	
	0.6	11.0	π/2	0.02	Gravel pavement	
[27]	− 1.0	11.5	π/2	0.04	NG	South of the Beiluhe Basin on the QTP
	4.1	10.6	π/2	0.04	SS	
	0.1	12.0	π/2	0.04	NS	
	5.3	15.6	π/2	0.04	Asphalt pavement	

Table 3. A list of T_0 and A which have been used in simulated temperature of permafrost. "–" do not be measured, *NG* natural ground surface, *S* side slope, *SS* south-facing side slope, *NS* north-facing side slope, *QTR* Qinghai-Tibet Railway, *QTP* Qinghai-Tibet Plateau.

As a result, the TCM-predicted temperature is coincident with the observed ones. However, in most cases, T_0, A, and ϕ are unknown. Many documented articles states that T_0, A, and ϕ are estimated on the basis of the adhesive layer theory, in which both T_0 and A are some cesium degree greater than the local air temperature. But how to estimate both T_0 and A is seldom explained. Table 3 lists T_0, A, and ϕ that have been used to predict the temperature of permafrost under embankments in the Qinghai-Tibet Plateau. It can be seen that the T_0, A, and ϕ vary greatly and that their values, sometime, are specified empirically and randomly.

While the HFM does not need T_0, A, and ϕ, it needs to guess some parameters like sky clearness factor, solar reflectance and others. As the heat in the ground comes primarily from the sunlight, the most challenge of the HFM is to guess a reliable solar reflectance R on the upper surface. Although the R value of a surface can be measured, the true R value varies during the courses of day and year, with the lowest reflectance in summer and greatest value in winter[12]. It has been advocated that the use of energy-based R value to replace the true R so that the seasonal and daily variations of the solar reflectance at the embankment surface are weighed. The data for the energy-based R value, however, is very limited currently[28]. Specifying a reliable R value for the upper ground surface is thus challenged. Further studies are thus expected to understand the solar reflectance of ground surface in permafrost regions.

The application of the HFM. The HFM is helpful to select the right performance grading of an asphalt binder according to the climatic condition in the area of uses. In permafrost regions, asphalt pavement is preferred because its flexible properties are advantageously adapted to differential settlement that is caused by the warming of the underlying frozen soils[29]. Asphalt pavement is typically placed on the top of an embankment. It is critical to select the right performance grading of the asphalt binders to the right climate condition in the area of uses. Performance grading is a function of annual maximum and minimum pavement surface temperature,

with one being the average seven-day maximum pavement temperature and the other being the minimum[30,31]. With the HFM, these temperature extremes can be precisely estimated according to the texture and color of the asphalt pavement and to the specific climatic conditions.

The HFM is powerful to estimate the heat gain and loss at the embankment surface precisely. The most concern heat flux component at the ground surface is the conductive heat flux, which mainly determines the temperature of the underlying frozen soils[32–34]. The HFM can reliably estimate the conductive heat flux to an embankment in a specific climate condition. Under the context of global warming, the HFM can be a useful tool to envision if the underlying permafrost can be cooled by varying embankment surface properties like albedo and emissivity. In addition to the conductive heat flux, how the radiant heat flux partitions at the embankment surface can be calculated. Understanding the heat flux balance at the ground surface is crucial to develop cool embankments and cool pavements for preserving the underlying permafrost under global warming.

The HFM is robust to find practical solutions to eliminate the thermal asymmetry of a roadway embankment in permafrost regions. After an embankment is built, the southern side slope absorbs more solar irradiance than the northern one does. As a result, the permafrost under the southern side slope is typically some Celsius degrees warmer than that under the northern one, a phenomenon that is termed as the sunny-shady effect and has been blamed as the culprit to the longitudinal cracks of the embankment[35]. Since this effect is caused by differential solar irradiance on both embankment side slopes, it can be mitigated by increasing the albedo of the southern side slope. But it remains unknown that for a specific embankment, increasing the albedo of the southern side slope to which degree can equalize the heat gain of both side slopes and thus eliminate the sunny-shady effect. The HFM can fill this knowledge gap and serves as a powerful tool to estimate the sunny-shady effect.

The HFM is indispensable to precisely calculate the deformation of warming permafrost under the embankment. Building embankment alters the thermal regimes such that the embankment absorbs more sunlight than the adjacent natural ground surface even if the surface materials are the same[36]. Plus the construction thermal disturbance, the permafrost underlain a roadway embankment has been found 0–1 °C warmer than the adjacent natural ground, especially in warm permafrost regions[37]. It has been observed that this temperature increment has caused 10–20 cm settlement to the embankment in warm permafrost region, and that the warming of permafrost still continues due to the global warming[38]. Correctly simulating the temperature increment caused by global warming and construction-induced warming is crucial to predict the embankment's settlement, which is directly correlated to the damage of the embankment. As the HFM is far more reliable to predict the temperature of the underlying permafrost (Figs. 2 and 3), it is thus indispensable to foresee the serviceability of embankments in permafrost regions.

Other applications of the HFM may be vast but cannot be exhausted herein. For instance, the use of the HFM is not limited to the embankments in permafrost regions but also to those in seasonal frozen regions. It can be used to study on the influences of parameters like surface albedo, surface emissivity, surface roughness, pavement thermal inertia, and other controllable factors on the temperature of the underlying soils and of the pavement structures. It can be also adopted to estimate the impacts the uncontrollable factors like solar irradiance, wind speed, air temperature, and others on the soil temperature. Furthermore, it can be employed to estimate the temperature under embankments that is proactively cooled by inserting the embankment with thermosyphons, covering the side slope with crushed rock layer, and embedding the embankment with air convective duct, etc. While other applications of the HFM is unlimited and await further studies, this study is just a starting of the use of HFM to predict the temperature of permafrost under a roadway embankment.

Conclusion

This study proposed a heat-flux model (HFM) for the heat transfer at the upper surface of an embankment in permafrost regions. Different from traditional temperature-controlled model (TCM) that considers the annual ground-surface temperature varied as a sinusoidal wave, the HFM jointly considers the solar irradiance, heat convection, and thermal irradiance on the ground surface, as well as the shading effect of the embankment on the adjacent ground. The HFM model thus can be used to predict the influence of ground-surface thermal properties and local weather on the temperature of the permafrost under an embankment. The permafrost temperature predicted by HFM is compared against that observed ones. It is found that the HFM model can predict the permafrost soils' temperature precisely, for instance, with $R^2 = 0.975$, a mean error of 0.134 °C and a standard deviation of 0.702 °C. In comparison, the TCM-predicted temperature is also compared against the observed one. It is found that TCM predicts the permafrost soil temperature in a lower accuracy.

Temperatures predicted by the HFM are 0.1–0.2 °C lower than those predicted by the TCM, but the temperature-varying trend and temperature contour are similarly. It is concluded that if the temperature trend of the soil under an embankment is of concern, the TCM can be recommended if the mean annual ground-surface temperature and its amplitude can be guessed precisely. If the sensitivity of the weather data and ground-surface thermal properties on the permafrost temperature is of concern, the HFM is recommended but the solar reflectance of the ground surface must be weighted wisely. Further studies are expected to understand the energy-based solar reflectance of the natural ground surface and of the embankment surface so that the solar absorption in the HFM is weighted precisely. The HFM can be applied to guide the selection of the performance grading of asphalt pavement in permafrost regions, to understand the heat partition on the embankment surface, to understand the sunny-shady effect of embankments, to calculate the deformation of embankment, and explore other applications related to the HFM.

Data availability

Some or all data, models, or code that support the findings of this study are available from the corresponding author upon reasonable request.

Received: 18 September 2021; Accepted: 27 January 2022
Published online: 02 August 2022

References

1. Ran, Y. *et al.* Distribution of permafrost in China: An overview of existing permafrost maps. *Permafrost Periglac.* **23**, 322–333. https://doi.org/10.1002/ppp.1756 (2012).
2. Ma, W. *et al.* Remedying embankment thaw settlement in a warm permafrost region with thermosyphons and crushed rock revetment. *Can. Geotech. J.* **49**, 1005–1014. https://doi.org/10.1139/t2012-058 (2012).
3. Wagner, A. M. *et al.* Permafrost degradation and subsidence observations during a controlled warming experiment. *Sci. Rep.* **8**, 10908. https://doi.org/10.1038/s41598-018-29292-y (2018).
4. Pei, W., Zhang, M., Li, S., Lai, Y. & Jin, L. Enhancement of convective cooling of the porous crushed-rock layer in cold regions based on experimental investigations. *Int. Commun. Heat Mass* **87**, 14–21. https://doi.org/10.1016/j.icheatmasstransfer.2017.06.019 (2017).
5. Shang, Y., Niu, F., Lin, Z. & Sun, T. Analysis of the cooling effect of a concrete thermal pile in permafrost regions. *Appl. Therm. Eng.* **173**, 115254. https://doi.org/10.1016/j.applthermaleng.2020.115254 (2020).
6. Lu, Q., Zhao, D. & Wu, S. Simulated responses of permafrost distribution to climate change on the Qinghai-Tibet Plateau. *Sci. Rep.* **7**, 3845. https://doi.org/10.1038/s41598-017-04140-7 (2017).
7. Sun, B., Yang, L., Liu, Q. & Xu, X. Numerical modelling for crushed rock layer thickness of highway embankments in permafrost regions of the Qinghai-Tibet Plateau. *Eng. Geol.* **114**, 181–190. https://doi.org/10.1016/j.enggeo.2010.04.014 (2010).
8. Sun, H., Ge, X., Zhu, D., Niu, F. & Chen, J. Numerical investigation of the temperature field of a new convection-intensifying composite embankment in permafrost regions. *J. Cold Reg. Eng.* **33**, 06018001. https://doi.org/10.1061/(ASCE)CR.1943-5495.0000174 (2019).
9. Han, F., Yu, W., Yi, X., Hu, D. & Lu, Y. Thermal regime of paved embankment in permafrost regions along the Qinghai-Tibet Engineering Corridor. *Appl. Therm. Eng.* **108**, 330–338. https://doi.org/10.1016/j.applthermaleng.2016.07.126 (2016).
10. Qin, Y., Hiller, J. E. & Bao, T. Modeling cold region ground temperatures with a heat flux upper boundary model. *J. Cold Reg. Eng.* **27**, 29–43. https://doi.org/10.1061/(ASCE)CR.1943-5495.0000051 (2013).
11. Qin, Y. & Bao, T. Modeling geothermal regime in the Qinghai-Tibet Plateau: An examination of the upper-boundary condition. *Arab. J. Geosci.* **7**, 855–864. https://doi.org/10.1007/s12517-013-0889-2 (2013).
12. Liu, Z., Chen, J., Jin, L., Zhang, Y. & Lei, C. Roadbed temperature study based on earth-atmosphere coupled system in permafrost regions of the Qinghai-Tibet Plateau. *Cold Reg. Sci. Technol.* **86**, 167–176. https://doi.org/10.1016/j.coldregions.2012.10.005 (2013).
13. Zhang, M., Lai, Y., Gao, Z. & Yu, W. Influence of boundary conditions on the cooling effect of crushed-rock embankment in permafrost regions of Qinghai-Tibetan Plateau. *Cold Reg. Sci. Technol.* **44**, 225–239. https://doi.org/10.1016/j.coldregions.2005.12.002 (2006).
14. Qin, Y. & Tang, P. Effects of diurnal temperature rhythm on the geothermal regime under the embankment in Qinghai-Tibet plateau. *Arab. J. Geosci.* **4**, 259–267. https://doi.org/10.1007/s12517-010-0166-6 (2011).
15. Zhu, L. Study of the adherent layer on different types of ground in permafrost regions on the Qinghai-Xizang plateau. *J. Glaciol. Geocryol.* **10**, 8–14 (In Chinese with English Abstract) (1988).
16. Qin, Y. & Hiller, J. E. Ways of formulating wind speed in heat convection significantly influencing pavement temperature prediction. *Heat Mass Transfer* **49**, 745–752. https://doi.org/10.1007/s00231-013-1116-0 (2013).
17. Orgill, J. F. & Hollands, K. G. T. Correlation equation for hourly diffuse radiation on a horizontal surface. *Sol. Energy* **19**, 357–359. https://doi.org/10.1016/0038-092X(77)90006-8 (1977).
18. Zhang, X., Yan, L.-E. & Qin, Y. Regulating solar absorptance for remedying thermal asymmetry of a roadway embankment. *Int. J. Heat Mass Tran.* **121**, 64–71. https://doi.org/10.1016/j.ijheatmasstransfer.2017.12.151 (2018).
19. Qin, Y., Tan, K., Yang, H. & Li, F. The albedo of crushed-rock layers and its implication to cool roadbeds in permafrost regions. *Cold Reg. Sci. Technol.* **128**, 32–37. https://doi.org/10.1016/j.coldregions.2016.05.004 (2016).
20. Lai, Y., Wang, Q., Niu, F. & Zhang, K. Three-dimensional nonlinear analysis for temperature characteristic of ventilated embankment in permafrost regions. *Cold Reg. Sci. Technol.* **38**, 165–184. https://doi.org/10.1016/j.coldregions.2003.10.006 (2004).
21. Lai, Y., Zhang, S., Zhang, L. & Xiao, J. Adjusting temperature distribution under the south and north slopes of embankment in permafrost regions by the ripped-rock revetment. *Cold Reg. Sci. Technol.* **39**, 67–79. https://doi.org/10.1016/j.coldregions.2004.04.003 (2004).
22. Liu, Z., Lai, Y., Zhang, M. & Zhang, X. Numerical analysis for random temperature fields of embankment in cold regions. *Sci. China Ser. D* **50**, 404–410. https://doi.org/10.1007/s11430-007-2043-z (2007).
23. Zheng, B., Zhang, J. & Qin, Y. Investigation for the deformation of embankment underlain by warm and ice-rich permafrost. *Cold Reg. Sci. Technol.* **60**, 161–168. https://doi.org/10.1016/j.coldregions.2009.08.012 (2010).
24. Chen, L., Yu, W., Yi, X., Hu, D. & Liu, W. Numerical simulation of heat transfer of the crushed-rock interlayer embankment of Qinghai-Tibet Railway affected by aeolian sand clogging and climate change. *Cold Reg. Sci. Technol.* **155**, 1–10. https://doi.org/10.1016/j.coldregions.2018.07.009 (2018).
25. Su, B., Li, N. & Quan, X. The numerical study on the ventilated embankment in permafrost regions in Qinghai-Tibet railway. *Cold Reg. Sci. Technol.* **38**, 229–238. https://doi.org/10.1016/j.coldregions.2003.11.003 (2004).
26. Qian, J., Yu, Q., You, Y., Hu, J. & Guo, L. Analysis on cooling effect of new hollow concrete brick revetment under gravel pavement in permafrost regions. *Cold Reg. Sci. Technol.* **85**, 15–21. https://doi.org/10.1016/j.coldregions.2012.06.003 (2013).
27. Yuan, C., Yu, Q., You, Y. & Guo, L. Formation mechanism of longitudinal cracks in expressway embankments with inclined thermosyphons in warm and ice-rich permafrost regions. *Appl. Therm. Eng.* **133**, 21–32. https://doi.org/10.1016/j.applthermaleng.2017.12.118 (2018).
28. Sailor, D. J. & Fan, H. Modeling the diurnal variability of effective albedo for cities. *Atmos. Environ.* **36**, 713–725. https://doi.org/10.1016/S1352-2310(01)00452-6 (2002).
29. Duojie, C. *et al.* Assessment of freeze-thaw cycles impact on flexural tensile characteristics of asphalt mixture in cold regions. *Math. Probl. Eng.* **2021**, 6697693. https://doi.org/10.1155/2021/6697693 (2021).
30. Ramadhan, R. H. & Al-Abdul Wahhab, H. I. Temperature variation of flexible and rigid pavements in Eastern Saudi Arabia. *Build. Environ.* **32**, 367–373. https://doi.org/10.1016/S0360-1323(96)00072-8 (1997).
31. Hao, J., Cao, P., Liu, Z., Wang, Z. & Xia, S. Developing of a SBS polymer modified bitumen to avoid low temperature cracks in the asphalt facing of a reservoir in a harsh climate region. *Constr. Build. Mater.* **150**, 105–113. https://doi.org/10.1016/j.conbuildmat.2017.05.200 (2017).
32. Qin, Y., Liang, J., Huang, Z. & Tan, K. Painting the roadway embankment with non-white high reflective pigments to raise the albedo. *Environ. Earth Sci.* **75**, 359. https://doi.org/10.1007/s12665-016-5273-6 (2016).
33. Wang, Q., Fang, J., Zhao, X. & Hu, K. The influence of pavement type on the thermal stability of block-stone embankments in the warm permafrost region. *Transp. Geotech.* **23**, 100334. https://doi.org/10.1016/j.trgeo.2020.100334 (2020).
34. Liu, J., Tai, B. & Fang, J. Ground temperature and deformation analysis for an expressway embankment in warm permafrost regions of the Tibet plateau. *Permafrost Periglac.* **30**, 208–221. https://doi.org/10.1002/ppp.2007 (2019).

35. Wang, S. *et al.* The temporal effect of distress developments of frozen embankments in the permafrost regions along the Qinghai-Tibet Highway. *J. Test. Eval.* **47**, 3059–3079. https://doi.org/10.1520/JTE20170487 (2018).
36. Qin, Y., Huang, H., Ying, J. & Yang, T. Simulation of short-wave solar radiative transfer across a roadway embankment. *Int. J. Heat Mass Tran.* **108**, 332–340. https://doi.org/10.1016/j.ijheatmasstransfer.2016.11.093 (2017).
37. Qin, Y. & Li, G. Permafrost warming under the earthen roadbed of the Qinghai-Tibet Railway. *Environ. Earth Sci.* **64**, 1975–1983. https://doi.org/10.1007/s12665-011-1014-z (2011).
38. Qin, Y., Zhang, J., Li, G. & Qu, G. Settlement characteristics of unprotected embankment along the Qinghai-Tibet Railway. *Cold Reg. Sci. Technol.* **60**, 84–91. https://doi.org/10.1016/j.coldregions.2009.08.002 (2010).
39. Anderson, D. M. & Tice, A. R. Predicting unfrozen water contents in frozen soils from surface area measurements. *High. Res. Rec.* **393**, 12–18 (1972).

Acknowledgements

This work is jointly supported by the high-level innovation team and outstanding scholar program in Guangxi colleges and the Science Foundation of Guangxi (No. 2018GXNSFAA294070, 2018GXNSFDA138009).

Author contributions

T.W. and L.Y. wrote the manuscript text together and T.W. prepared the numerical simulation and all figures. All authors reviewed the manuscript.

Competing interests

The authors declare no competing interests.

Additional information

Supplementary Information The online version contains supplementary material available at https://doi.org/10.1038/s41598-022-17529-w.

Correspondence and requests for materials should be addressed to T.W.

Reprints and permissions information is available at www.nature.com/reprints.

Publisher's note Springer Nature remains neutral with regard to jurisdictional claims in published maps and institutional affiliations.